



THE UNIVERSITY *of* EDINBURGH

Edinburgh Research Explorer

Resolution-doubled one-dimensional wavelength modulation spectroscopy tomography for flame flatness validation of a flat-flame burner

Citation for published version:

Liu, C, Xu, L, Li, F, Cao, Z, Tsekenis, SA & McCann, H 2015, 'Resolution-doubled one-dimensional wavelength modulation spectroscopy tomography for flame flatness validation of a flat-flame burner' Applied Physics B: Lasers and Optics, vol. 120, no. 3, pp. 407-416. DOI: 10.1007/s00340-015-6150-9

Digital Object Identifier (DOI):

[10.1007/s00340-015-6150-9](https://doi.org/10.1007/s00340-015-6150-9)

Link:

[Link to publication record in Edinburgh Research Explorer](#)

Document Version:

Publisher's PDF, also known as Version of record

Published In:

Applied Physics B: Lasers and Optics

General rights

Copyright for the publications made accessible via the Edinburgh Research Explorer is retained by the author(s) and / or other copyright owners and it is a condition of accessing these publications that users recognise and abide by the legal requirements associated with these rights.

Take down policy

The University of Edinburgh has made every reasonable effort to ensure that Edinburgh Research Explorer content complies with UK legislation. If you believe that the public display of this file breaches copyright please contact openaccess@ed.ac.uk providing details, and we will remove access to the work immediately and investigate your claim.



Resolution-doubled one-dimensional wavelength modulation spectroscopy tomography for flame flatness validation of a flat-flame burner

Chang Liu¹ · Lijun Xu¹ · Fangyan Li¹ · Zhang Cao¹ · Stylianos A. Tsekenis² · Hugh McCann²

Received: 15 April 2015 / Accepted: 26 May 2015 / Published online: 11 June 2015
© Springer-Verlag Berlin Heidelberg 2015

Abstract Flame flatness is one of the most critical factors in evaluating the performance of a flat-flame burner. In this paper, the flame flatness of a flat-flame burner is validated using a resolution-doubled one-dimensional wavelength modulation spectroscopy tomography (1D-WMST) technique that only uses one view of multiple parallel laser beams. When the interval of two neighboring parallel laser beams is Δr , a designed novel geometry of the parallel laser beams realizes a doubled tomographic resolution of $\Delta r/2$. Using the proposed technique, the distributions of temperature and H_2O mole fraction in an axisymmetric premixed flame are simultaneously reconstructed and hence the flame flatness of a flat-flame burner can be validated. The flatness factor is quantitatively described by the similarity between the reconstructed and expected distributions of H_2O mole fraction. For flat and non-flat flames, the experimental results agree well with the CFD simulation results, denoting that the resolution-doubled 1D-WMST technique provides a noninvasive, reliable and low cost way to validate the flame flatness of the flat-flame burner.

1 Introduction

As a standard device to produce flat premixed flames, flat-flame burners are widely used to investigate combustion

mechanisms and heat transfer processes [1, 2]. They are also used as important combustion devices in development and calibration of optical diagnostic techniques [3–7]. Generally, the premixed flame of the flat-flame burner is axisymmetric and assumed to be flat in a radial direction. In other words, distributions of temperature and mole fractions of chemical species on a cross section of the flame are assumed to be uniform in the radial direction. The flame flatness is one of the most critical factors in evaluating the performance of the flat-flame burner. On the one hand, when calibrating optical diagnostic instruments, a clear separation is required between the region of interest, i.e., the core flame, and the regions which are not of interest, i.e., surrounding air. On the other hand, to obtain accurate flame parameters from equilibrium calculations, temperature and mole fractions of chemical species are required to be as constant as possible throughout the core flame. Therefore, the flat-flame burner should be well designed to ensure the flame as flat as possible.

To produce a flat flame, the burner plug is always ringed with shrouding nitrogen to isolate core flame from air disturbance [4, 8]. However, the effects of heat transfer between the core flame and the cold boundary of air are inevitable, which lead to non-uniform distributions of temperature and mole fractions of chemical species in the radial direction. For instance, due to the diffusion of the unburned fuel into surroundings, temperature-uniform area was reduced at sub-atmospheric pressures, and the laminar burning velocities dropped down [9]. In addition, the material of the burner plug plays an important role in affecting the flame flatness. For rich premixed flame produced by the McKenna burner with a stainless steel plug, the flame is not as flat as that with a bronze plug, which is mainly caused by the difference of thermal conductivity for two cases [10]. Therefore, to examine the performance of the

✉ Lijun Xu
lijunxu@buaa.edu.cn

¹ Ministry of Education's Key Laboratory of Precision Opto-Mechatronics Technology, School of Instrument Science and Opto-Electronic Engineering, Beihang University, Beijing, China

² School of Engineering, University of Edinburgh, Edinburgh EH9 3JL, UK

flat-flame burner, it is necessary to validate the flame flatness of the flat-flame burners.

The flame flatness can be described by uniformity of the distributions of temperature and mole fractions of chemical species, which were commonly obtained using non-intrusive optical diagnostic techniques in the past decades [8, 10]. For instance, Fuyuto et al. [11] employed the laser-induced fluorescence (LIF) technique to measure the distributions of temperature and mole fractions of chemical species in the quenching boundary layer of a flat-flame burner. By applying corrections for the temperature dependence of scattering cross section, Sutton et al. [5] calibrated a McKenna burner with a high-accuracy Rayleigh scattering thermometry system. In addition, Prucker et al. [8] used coherent anti-Stokes Raman scattering (CARS) technique to measure the temperature distributions of the H₂/air premixed flames with different stoichiometries, flow rates and heights above the burner plug. Although these attempts can be used to validate the flatness of a flame, the experimental systems require complicated optics, expensive laser sources and clean operating environment, normally a clean room, which are sometimes difficult to meet.

Wavelength modulation spectroscopy (WMS) is a robust, sensitive and low cost technique for temperature measurement and chemical species detection with good noise-tolerant characteristics [12–16]. By combining WMS with tomography techniques, the distributions of temperature and mole fractions of chemical species can be reconstructed. Because the flame produced by the flat-flame burner under normal conditions is axisymmetric, the typical tomography modalities, each with multiple views and projections [17–21], can be simplified as one-dimensional tomography that only uses one view of multiple parallel beams [22, 23].

In this paper, a resolution-doubled one-dimensional wavelength modulation spectroscopy tomography (1D-WMST) technique is proposed to reconstruct the distributions of temperature and mole fractions of chemical species in the premixed flame. By specially designing the geometry of the parallel laser beams, the tomographic resolution can be doubled up to $\Delta r/2$ when the interval of two neighboring parallel laser beams is Δr . With the reconstructed results in hand, the similarity between the reconstructed and expected distributions of mole fractions is used to describe the flame flatness.

2 Methodology

Wavelength modulation spectroscopy is well established for accurate measurements of temperature and mole fractions of chemical species. Particularly, gas properties and absorption lineshapes can be retrieved by fitting the first

harmonic-normalized second harmonic, i.e., WMS-2f/1f, of the modulated absorption signals, even in harsh environments with flame fluctuation, emission and non-absorption attenuation [24, 25]. By combining WMS with one-dimensional tomography, the resolution-doubled 1D-WMST technique with a designed novel geometry of the parallel laser beams is introduced and used to reconstruct the distributions of temperature and mole fractions of chemical species of the axisymmetric flame in the radial direction.

2.1 Fundamentals of wavelength modulation spectroscopy

To introduce the theory of resolution-doubled 1D-WMST in Sect. 2.3, we briefly review the theory of WMS, which has been extensively discussed in the literature [12, 15]. By imposing a high-frequency sinusoidal modulation signal on a relatively low frequency wavelength-scanning signal, the laser frequency $\nu(t)$ can be expressed as

$$\nu(t) = \bar{\nu}(t) + a \cos(2\pi f_m t + \varphi), \quad (1)$$

where $\bar{\nu}(t)$ is the scanning laser frequency, φ the initial phase of the frequency modulation (FM), a and f_m the modulation depth and modulation frequency, respectively.

The incident laser intensity $I(t)$ is modeled by

$$I(t) = \bar{I}_0 [1 + i_1 \cos(2\pi f_m t + \varphi_1) + i_2 \cos(4\pi f_m t + \varphi_2)], \quad (2)$$

where \bar{I}_0 is the average laser intensity at center frequency $\bar{\nu}$, i_1 the amplitude of linear intensity modulation (IM), φ_1 the phase shift between the FM and IM, and i_2 the amplitude of nonlinear IM with phase shift φ_2 .

The wavelength-dependent transmission coefficient $\tau(\nu)$ for an isolated transition is given by the Beer–Lambert’s law,

$$\tau(\nu) = \frac{I_t}{I_0} = e^{-\alpha(\nu)} = e^{-A\phi}, \quad (3)$$

where I_t and I_0 are the transmitted and incident laser intensities, respectively. $\alpha(\nu)$ is the absorbance of the transition, which is determined by the integrated absorbance area A and the lineshape function ϕ .

For a laser path with non-uniform distributions of temperature and mole fractions of chemical species, the integrated absorbance area A can be expressed as

$$A = \int_{-\infty}^{\infty} \alpha d\nu = \int_0^L X_{\text{abs}}(x) S[T(x)] dl, \quad (4)$$

where $T(x)$ is the local temperature, $X_{\text{abs}}(x)$ the local mole fraction of the absorbing species, $S[T(x)]$ the temperature-dependent line strength of the transition, L the optical absorbing path length.

After wavelength modulation, $\tau(t)$ is an even function in $2\pi f_m t$, which can be expanded into Fourier cosine series:

$$\tau(t) = \sum_{n=0}^{n=+\infty} H_n(\bar{\nu}, a) \cos(n \cdot 2\pi f_m t), \quad (5)$$

where $H_n(\bar{\nu}, a)$ are the n th-order harmonic coefficients given by

$$H_0(\bar{\nu}, a) = \frac{1}{2\pi} \int_{-\pi}^{+\pi} \tau(\bar{\nu} + a \cos\theta) \cdot d\theta, \quad (6)$$

$$H_n(\bar{\nu}, a) = \frac{1}{\pi} \int_{-\pi}^{+\pi} \tau(\bar{\nu} + a \cos\theta) \cdot \cos n\theta \cdot d\theta. \quad (7)$$

By multiplying the detector signal with a sinusoidal reference signal at f_m and $2f_m$, the magnitudes of the first harmonic and the second harmonic of the modulated absorption signals, noted as S_{1f} and S_{2f} , can be isolated by digital lock-in and low-pass filter and given by

$$S_{1f} = \sqrt{X_{1f}^2 + Y_{1f}^2}, \quad (8)$$

$$S_{2f} = \sqrt{X_{2f}^2 + Y_{2f}^2}, \quad (9)$$

where X_{1f} , X_{2f} , Y_{1f} and Y_{2f} are the X and Y components of the first-harmonic and second-harmonic signals, respectively. X_{1f} , X_{2f} , Y_{1f} and Y_{2f} can be expressed as follows:

$$X_{1f} = \frac{G\bar{I}_0}{2} \left[H_1 + i_1 \left(H_0 + \frac{H_2}{2} \right) \cos(\varphi_1 - \varphi) + \frac{i_2}{2} (H_1 + H_3) \cos(\varphi_2 - \varphi) \right], \quad (10)$$

$$Y_{1f} = \frac{G\bar{I}_0}{2} \left[i_1 \left(H_0 - \frac{H_2}{2} \right) \sin(\varphi_1 - \varphi) + \frac{i_2}{2} (H_1 - H_3) \sin(\varphi_2 - \varphi) \right], \quad (11)$$

$$X_{2f} = \frac{G\bar{I}_0}{2} \left[H_2 + \frac{i_1}{2} (H_1 + H_3) \cos(\varphi_1 - \varphi) + i_2 \left(H_0 + \frac{H_4}{2} \right) \cos(\varphi_2 - \varphi) \right], \quad (12)$$

$$Y_{2f} = \frac{G\bar{I}_0}{2} \left[\frac{i_1}{2} (H_1 - H_3) \sin(\varphi_1 - \varphi) + i_2 \left(H_0 - \frac{H_4}{2} \right) \sin(\varphi_2 - \varphi) \right], \quad (13)$$

where G is the electro-optical gain of the detection system and the laser transmission losses due to scattering and beam steering.

By normalizing the second-harmonic signal with the first-harmonic signal, hardware-related parameters of the detection system, such as the laser intensity, detector sensitivity, signal amplification coefficient, lock-in gain, can be eliminated. Therefore, the WMS-2f/1f, noted as $S_{2f/1f}$, is only a function of the gas parameters, i.e., A and ϕ , and the laser parameters, i.e., a , i_1 and i_2 , which are expressed as follows:

$$S_{2f/1f} = \sqrt{X_{2f}^2 + Y_{2f}^2} / \sqrt{X_{1f}^2 + Y_{1f}^2} = f(A, \phi, a, i_1, i_2). \quad (14)$$

2.2 Fitting of WMS-2f/1f

To avoid characterizing the complex analytic model of laser intensity in Eq. (2), fitting of WMS-2f/1f was recently developed [24, 25]. By fitting a simulated WMS-2f/1f to a measured WMS-2f/1f, the gas parameters can be accurately calculated even in large optical depth and modulation depth. The basic steps of the technique are listed as follows:

1. The laser penetrates the target species, and the transmitted laser intensity $^M I_t(t)$ is measured.
2. By extracting S_{2f} of $^M I_t(t)$, the absolute center frequency of the transition, which corresponds to the peak of S_{2f} , can be located. Then, using an etalon with FSR of 0.015 cm^{-1} , the frequency-modulated response in Eq. (1) can be characterized and the laser parameters in Eq. (14) can be obtained.
3. By assuming A and ϕ , the simulated absorbance $^S \alpha(\nu)$ can be obtained from Eq. (3). In general, A is calculated from Eq. (4), while ϕ is described by the Voigt lineshape. As elaborated in our previous work, the Voigt lineshape can be fast calculated from the combinations of the Gauss full width at half maximum (FWHM) and Lorentz FWHM [7]. After wavelength modulation, $^S \alpha(\nu(t))$ can be obtained given the frequency-modulated response in step 2.
4. The incident laser intensity $^M I_0(t)$ is measured in the absence of the absorption species. Given $^M I_0(t)$ and $^S \alpha(\nu(t))$, the simulated transmitted laser intensity $^S I_t(t)$ can be calculated by

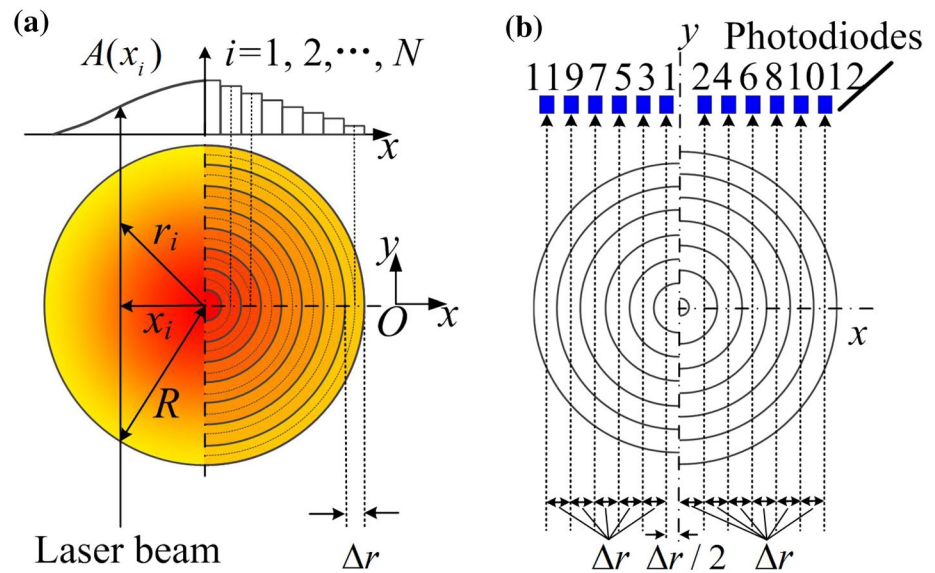
$$^S I_t(t) = ^M I_0(t) \cdot e^{-\alpha(\nu(t))}. \quad (15)$$

5. The digital lock-in and low-pass filter are used to obtain the first and second harmonics of $^S I_t(t)$ and $^M I_t(t)$, noted as $^S S_{1f}$, $^M S_{1f}$, $^S S_{2f}$ and $^M S_{2f}$, respectively. According to Eq. (14), the simulated and measured WMS-2f/1f, noted as $^S S_{2f/1f}$ and $^M S_{2f/1f}$, can be further obtained. By least-squares fitting $^S S_{2f/1f}$ to $^M S_{2f/1f}$ the gas parameters, i.e., A and ϕ , can be obtained.

2.3 Resolution-doubled 1D-WMST

To realize the resolution-doubled 1D-WMST technique, a concentric circles-based model and a coordinate system are

Fig. 1 Geometry of **a** axisymmetric flame and **b** parallel laser beams in the resolution-doubled 1D-WMST technique



established, as shown in Fig. 1a. The origin of the coordinate system is at the center of the flame with radius R . The flame is discretized into N equal-spaced concentric circles. The interval of two adjacent concentric circles is $\Delta r = R/(N - 0.5)$. The radius of the i th concentric circle is $r_i = i\Delta r$, $i = 1, \dots, N$. As the flame is axisymmetric, the pressure, temperature and mole fraction of a chemical species in the i th circle are uniform, noted as $P(r_i)$, $T(r_i)$ and $X(r_i)$. The density of the integrated absorbance $a(r_i)$ can be expressed as

$$a(r_i) = P(r_i) \cdot S[T(r_i)] \cdot X(r_i). \quad (16)$$

N parallel laser beams, with interval Δr , penetrate the cross section of the flame along the direction of positive y axis. The coordinate of the intersection of the i th laser beam and x axis is $x_i = i\Delta r$, $i = 1, \dots, N$. Therefore, the relationship between the integrated absorbance area $A(x_i)$ and $a(r_i)$ can be given by the Abel's integral equation,

$$A(x_i) = 2 \sum_{j=i}^N \int_{r_j - \Delta r/2}^{r_j + \Delta r/2} \frac{a(r_j) \tilde{r}}{\sqrt{\tilde{r}^2 - x_i^2}} d\tilde{r}, \quad (17)$$

where $A(x_i)$ is obtained by fitting WMS-2f/1f. Through Abel inversion, $a(r_i)$ can be solved by

$$a(r_i) = -\frac{1}{\pi} \int_{r_i - \Delta r/2}^{r_i + \Delta r/2} \frac{A'(x_j + \delta)}{\sqrt{(x_j + \delta)^2 - r_i^2}} d\delta, \quad (18)$$

where $A(x_i)$ is approximated into a quadratic form in the neighbor of x_i , noted as the three-point Abel deconvolution [22],

$$A'(x_i + \delta) = \frac{A(x_{i+1}) - A(x_{i-1}))}{2\Delta r} + \frac{A(x_{i+1}) + A(x_{i-1}) - A(x_i)}{\Delta r^2} \cdot \delta. \quad (19)$$

Using the two-color absorption spectroscopy strategy, the radial distribution of temperature $T(r_i)$ can be retrieved from Eq. (20),

$$T(r_i) = \frac{\frac{hc}{k}(E_2'' - E_1'')}{\ln \frac{a_1(r_i)}{a_2(r_i)} + \ln \frac{S_2(T_0)}{S_1(T_0)} + \frac{hc}{k} \frac{(E_2'' - E_1'')}{T_0}}. \quad (20)$$

To ensure good temperature sensitivity, the lower energy states of the selected two transitions, i.e., E_1'' and E_2'' should be of enough difference. With $T(r_i)$ in hand, the distribution of mole fraction of chemical species $X(r_i)$ can be calculated at an atmosphere pressure as follows:

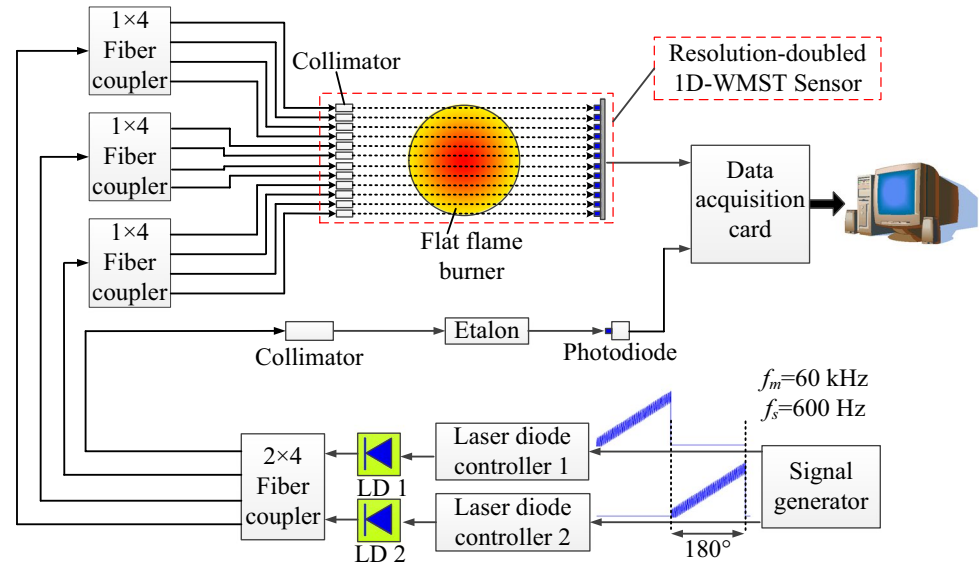
$$X(r_i) = \frac{a_1(r_i)}{S_1[T(r_i)]}. \quad (21)$$

In traditional 1D tomography, the parallel laser beams with spatial sampling interval of Δr penetrate the left or right half of the flame and provide a tomographic resolution of Δr . If the number of laser beams is large enough, the spatial sampling interval is equivalent to the tomographic resolution [26]. To increase the resolution, a novel geometry of the parallel laser beams is designed, as shown in Fig. 1b. The laser beams $\{l_i | i = 1, \dots, N\}$ are arranged as follows:

1. Given that N is an even number, the odd-numbered laser beams $\{l_i | i = 1, 3, 5, \dots, N - 1\}$ and the even-numbered laser beams $\{l_i | i = 2, 4, 6, \dots, N\}$ are sequentially arranged in the left and right sides of y axis, respectively.
2. For the odd-numbered or the even-numbered laser beams, the interval of two neighboring parallel laser beams is Δr .
3. The interval between the y axis and the laser beam l_1 is $\Delta r/2$, while that between the y axis and the laser beam l_2 is Δr .

Table 1 H₂O transitions selected in experiment

Transition index	Frequency ν_0 (cm ⁻¹)	S at 300 K (cm ⁻² atm ⁻¹)	S at 1000 K (cm ⁻² atm ⁻¹)	E'' (cm ⁻¹)
1	7185.6	1.96×10^{-2}	2.60×10^{-2}	1045.06
2	7444.35 + 7444.37 combined	1.10×10^{-3}	2.09×10^{-2}	1774.75 1806.67

Fig. 2 Schematic of the 1D-WMST system. The central frequencies of laser diode (LD) 1 and LD2 are 7185.6 and 7444.36 cm⁻¹, respectively

Because the flame is axisymmetric, the projections obtained from odd-numbered laser beams can be mirrored to the right of y axis. The mirrored projections and the even-numbered projections interlace with each other in the right side of the coordinate system. Thus, the actual interval between two neighboring projections among the combined projections is $\Delta r/2$. Therefore, the tomographic resolution is doubled up to $\Delta r/2$, although the smallest interval of two neighboring parallel laser beams in the real geometry is Δr .

3 Results and discussions

3.1 Selection of transitions

Water vapor (H₂O) is the main combustion product of the premixed flame. Therefore, the distributions of temperature and H₂O mole fraction were used to validate the flame flatness of the flat-flame burner. In the near-infrared spectrum range, many pairs of H₂O transitions have moderate line strength and good temperature sensitivity. Using the two-color absorption spectroscopy strategy, the H₂O transitions at 7185.6 and 7444.36 cm⁻¹ (7444.35 cm⁻¹ combined with 7444.37 cm⁻¹) were used to calculate the temperature and H₂O mole fraction. The characteristics of the selected transitions are listed in Table 1, respectively. It should be noted that although the selected transitions may not be the

optimum choices in the near-infrared spectrum range, good temperature sensitivity can be acquired for the given temperature range in the experiment [23, 27, 28]. Furthermore, the selected transitions were accessed by the distributed feedback diode (DFB) lasers available in our laboratory.

3.2 Experimental system

DFB laser diodes with linewidth of 10 MHz and output power of 5mW were used to generate the tunable laser at 7185.6 and 7444.36 cm⁻¹. Each of them was independently controlled with a laser diode controller by adjusting temperature and injection current. As shown in Fig. 2, the output laser at 7185.6 and 7444.36 cm⁻¹ was combined and split into four channels using a 2×4 fiber coupler. Two DFB laser diodes worked with a time-division multiplexing scheme [7, 23]. To be more specific, the injection current of each DFB laser diode was scanned with a sinusoidal signal at $f_m = 60$ kHz superposed on a linear ramp signal at $f_s = 600$ Hz, which were generated by a multi-channel arbitrary signal generator. The phase difference of scanning signals for the DFB laser diodes was 180°. In other words, one DFB laser diode was scanned during a scanning period, while the injection current was set under the lower working threshold for another DFB laser diode.

Subsequently, to monitor the laser frequency $\nu(t)$ during the wavelength scanning, the laser in the first channel

was collimated and delivered into an etalon with FSR of 0.015 cm^{-1} . Each laser in the other three channels was split into four channels using a 1×4 fiber coupler and then collimated. Twelve parallel laser beams with their geometry designed in Fig. 1b penetrated the premixed flame generated by a McKenna burner. In the experiment, the radius of the computation domain R was 35 mm. Therefore, a doubled tomographic resolution of 2.8 mm was realized when the minimum interval of two neighboring parallel laser beams is 5.6 mm. Finally, the transmitted laser intensities $^M I_t(t)$ were detected by 12 InGaSn PIN photodiodes with bandwidth of 10 MHz. The sensitive wavelength of the InGaSn PIN photodiode is 900–2050 nm, which covers the wavelengths of the laser. The signals of the 12 photodiodes were simultaneously sampled by a data acquisition card with 6 Msps. As noted in Sect. 2.2, the incident laser intensity $^M I_0(t)$ should be measured in the absence of the absorption species. Therefore, a nitrogen-purified path was provided to eliminate the interference absorption by H_2O in room air. It should be noted that the resolution-doubled 1D-WMST technique is based on accurately locating the parallel laser beams. Otherwise, noise will be added to the reconstruction results. To align and center the laser beams, both the collimators and the photodiode arrays were mounted on optical adjustable brackets with a precision of 0.02 mm. The measurement was implemented after the laser beams were accurately located.

3.3 Experimental results

3.3.1 Acquisition of the projection data

In the experiment, each laser diode was scanned around the central frequency about 1 cm^{-1} with a 600-Hz ramp signal, and modulated at $f_m = 60\text{ kHz}$ with the modulation depth $a = 0.2\text{ cm}^{-1}$. As shown in Fig. 3, using time-division multiplexing scheme, the transmitted laser intensities $^M I_t(t)$ of the transitions at 7185.6 and 7444.36 cm^{-1} were obtained with a repetition frequency of 300 Hz. In this way, the incident laser intensities $^M I_0(t)$ were measured in the nitrogen-purified path.

Then, the $^M S_{2f}$ and $^M S_{1f}$ were extracted from $^M I_t(t)$ with a 2-kHz Butterworth filter. The filter was also used to obtain the simulated WMS signals, i.e., $^S S_{2f}$ and $^S S_{1f}$. After characterizing the frequency-modulated responses of the laser diodes, the $^M S_{2f/1f}$ was calculated with $^M S_{2f}$ and $^M S_{1f}$ in hand. By assuming the simulated absorbance, the integrated absorbance areas $\tilde{A}(x_j)$ were inferred from fitting $^S S_{2f/1f}$ to $^M S_{2f/1f}$. Figure 4a–d shows the results of fitting $^S S_{2f/1f}$ to $^M S_{2f/1f}$ for the transitions at 7185.6 and 7444.36 cm^{-1} , respectively. Furthermore, after the fitting was converged, the simulated absorbance at the scanning laser frequency $\bar{\nu}$ and modulated laser frequency ν were inferred, as shown in Fig. 4e and f, respectively.

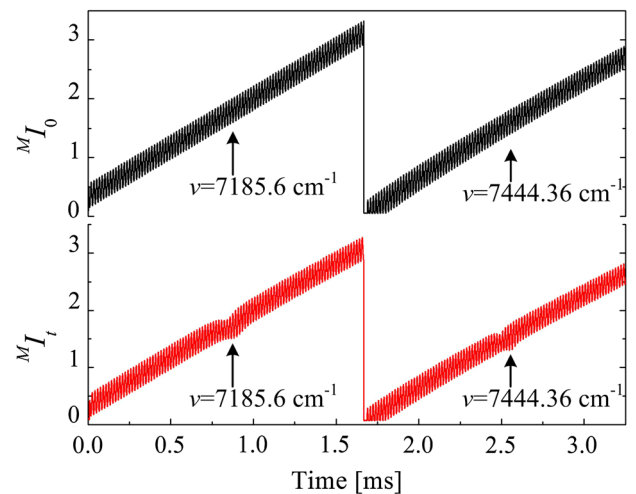


Fig. 3 Transmitted laser intensities $^M I_t(t)$ and incident laser intensities $^M I_0(t)$ of the transitions at 7185.6 and 7444.36 cm^{-1} within a scanning period

3.3.2 Flame Reconstruction

To validate the resolution-doubled 1D-WMST technique, the distributions of temperature and H_2O mole fraction in the radial direction were reconstructed and compared with those obtained using CFD simulation. In the simulation, a two-dimensional computation domain of the McKenna burner was established. The model was the same as a vertical section along z axis of McKenna burner, as shown in Fig. 5. The well-premixed fuel, i.e., methane and air, was released through the porous sintered bronze burner plug with diameter of 60 mm. Then, the fuel was ignited above the burner plug. To protect the flame from air convection, shrouding nitrogen was released from the shroud ring. Using the embedded semiautomatic meshing tool, the computation domain was discretized into 5030 nodes. The CFD simulation was implemented by utilizing ANSYS FLUENT. In the simulation, all the mixture inlets were set as velocity inlets, while the output boundaries of the computation domain were set as pressure outlets with zero gauge pressure and backflow directions normal to the boundaries. The solver was defined as a two-dimensional pressure-based steady solver, in which the face pressure at the boundary is the same as the value specified in the pressure outlet. Because the flame parameters are related to heat transfer, the energy equations were involved in the simulation to calculate the energy in the model. The viscous model was specified as laminar in case of the laminar flame, while that was specified as a standard k-epsilon model in case of the turbulent flame caused by the excessive flow of shrouding nitrogen. The species transport and finite-rate chemistry as related to volumetric reactions were established. The volumetric

Fig. 4 Results of fitting WMS- $2f/1f$. For the transitions at 7185.6 and 7444.36 cm^{-1} , **a** and **b** show the residuals between the measured and best-fit $S_{2f/1f}$, **c** and **d** show the measured and best-fit $S_{2f/1f}$, **e** and **f** show the corresponding simulated absorbance profiles

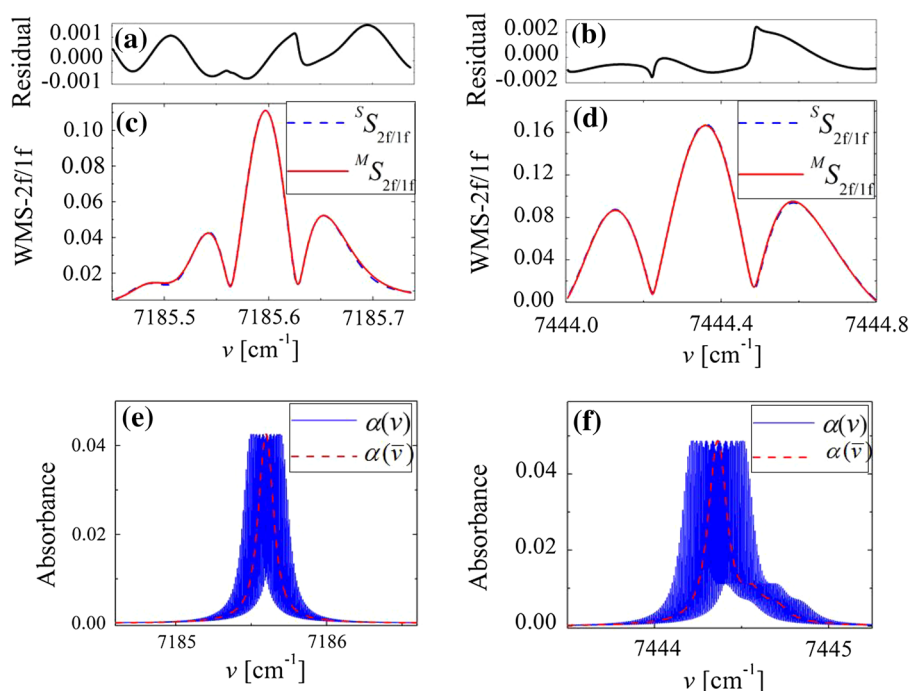
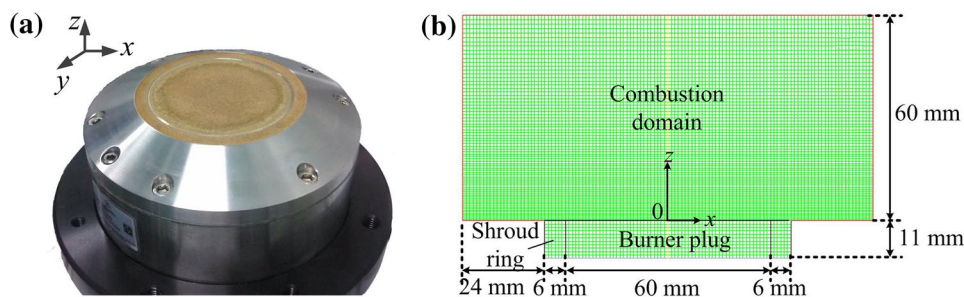


Fig. 5 **a** Photograph and **b** the two-dimensional computation domain of the McKenna burner



species are the multi-species used in the volumetric reactions. In detail, a methane–air mixture was selected in FLUENT including five relevant species, i.e., methane (CH_4), oxygen (O_2), carbon dioxide (CO_2), water (H_2O) and nitrogen (N_2). In the chemical reactions, the stoichiometric coefficients of CH_4 , O_2 , CO_2 and H_2O were set as 1, 2, 1 and 2, respectively. N_2 was not involved in the chemical reactions. The radiation heat transfer is calculated both in the regions of chemical reactions and in the regions of the burner plug.

Both in the simulation and the experiment, the equivalent ratio was 0.69 by setting the flow rates of methane and air to 1.1 and 15.25 L/min, respectively. The flow rate of shrouding nitrogen was set to 22.5 L/min. With above settings, a stable flame was generated. The height above the burner plug is noted as z . To validate the technique with different flame profiles, the laser beams were mounted at $z = 20$ and 40 mm, respectively. For 100 repetitive measurements, the reconstructed distributions of temperature,

${}^R T(r_i)$, and H_2O mole fraction, ${}^R X(r_i)$, and their standard deviations were obtained, as shown in Fig. 6a and b. The midpoint denotes the mean of the 100 solutions of ${}^R T(r_i)$ and ${}^R X(r_i)$, while the error bar to each midpoint denotes the standard deviation of the 100 solutions. The values between two neighboring midpoints are obtained from linear interpolation justified by the smooth variation of temperature and H_2O concentration. It can be seen that the uniform ranges of ${}^R T(r_i)$ and ${}^R X(r_i)$ at $z = 20$ mm are larger than those at $z = 40$ mm, denoting that the flame at $z = 20$ mm is more flat than that at $z = 40$ mm. Furthermore, if x is closer to 0, the three-point Abel deconvolution is more ill-posed, which results in larger standard deviations of ${}^R T(r_i)$ and ${}^R X(r_i)$. The weak absorptions around the boundary lead to smaller signal-to-noise ratio (SNR). Therefore, the standard deviations of ${}^R T(r_i)$ and ${}^R X(r_i)$ for $x > 30$ mm become larger with the increase in x .

To evaluate the performance of the technique, ${}^R T(r_i)$ and ${}^R X(r_i)$ were compared with those obtained using CFD

Fig. 6 Reconstructed and simulated distributions of temperature and H₂O mole fraction at the equivalent ratio of 0.69 and the flow rate of shrouding nitrogen of 22.5 L/min. **a** and **b** show the distributions of temperature and H₂O mole fraction obtained using the 1D-WMST technique and the CFD simulation. **c** and **d** show the contours of temperature and H₂O mole fraction in the vertical section of the flame at $y = 0$ obtained by the CFD simulation

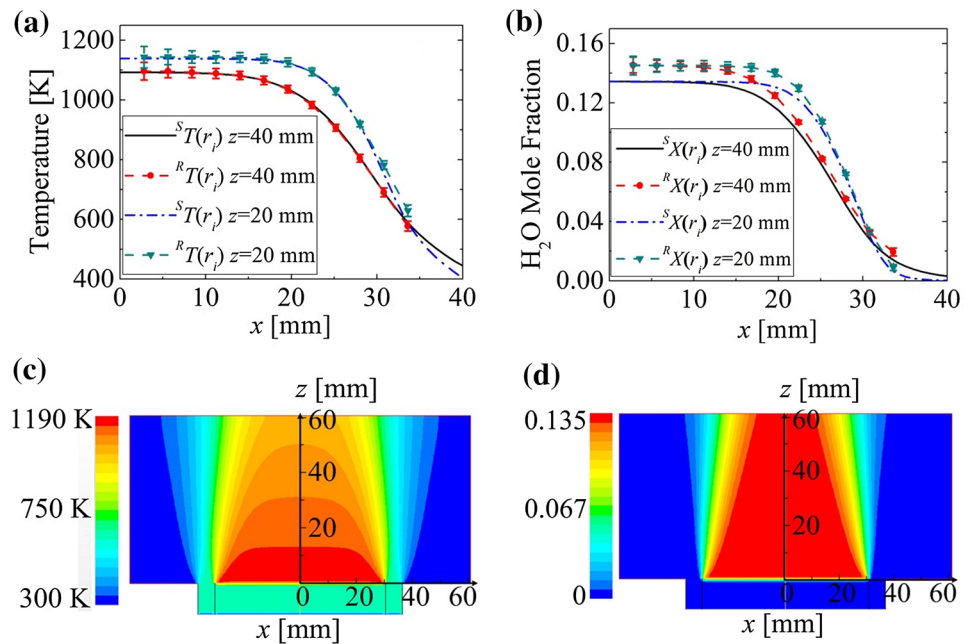
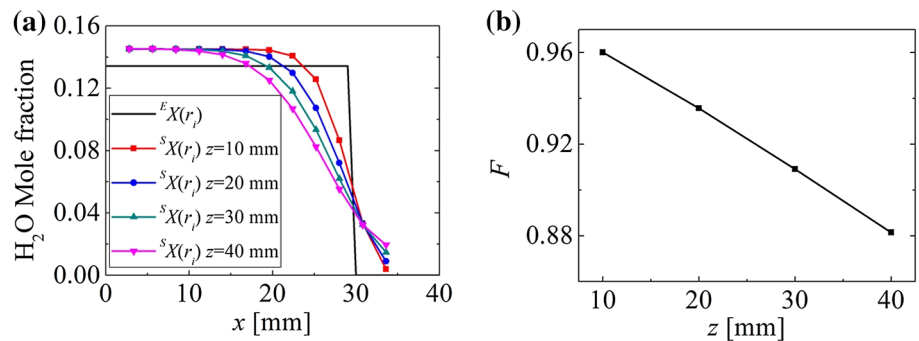


Fig. 7 Validation of the flame flatness. When the equivalent ratio was 0.69 and the flow rate of shrouding nitrogen was 22.5 L/min, **a** shows the expected and reconstructed distributions of H₂O mole fractions, while **b** depicts the flatness factor F of the flame at $z = 10, 20, 30, 40$ mm, respectively



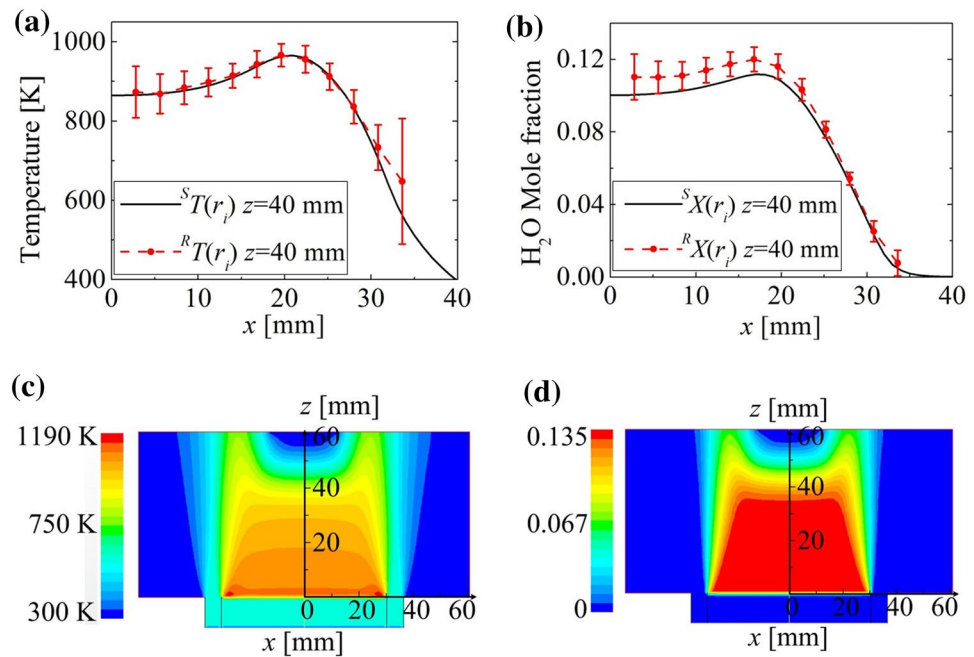
simulation. By setting the same combustion conditions with the experiment, the contours of temperature and H₂O mole fraction in the vertical section of the flame at $y = 0$ were obtained, as shown in Fig. 6c and d. Then, the simulated distributions of temperature, $^S T(r_i)$, and H₂O mole fraction, $^S X(r_i)$, along x axis at $z = 20$ mm and $z = 40$ mm were extracted. As shown in Fig. 6a and b, the mean values of $^R T(r_i)$ and $^R X(r_i)$ agree well with $^S T(r_i)$ and $^S X(r_i)$, denoting that the proposed technique is effective to reconstruct the distributions of the temperature and mole fraction of a chemical species in the premixed flame.

3.3.3 Validation of the flame flatness

Given an equivalent ratio, the expected H₂O mole fraction in the core flame can be obtained through equilibrium calculations. Moreover, a clear boundary is expected between the core flame and the surrounding air. However, due to inevitable heat transfer and air convection, deviations between the reconstructed and expected distributions of H₂O mole fraction, noted as $^R X(r_i)$ and $^E X(r_i)$, exist in practical applications, as shown in Fig. 7a. Therefore, the flatness factor F is quantitatively described in Eq. (6) by the similarity between $^R X(r_i)$ and $^E X(r_i)$.

$$F = \frac{N \sum_{i=1}^N {}^R X(r_i) {}^E X(r_i) - \sum_{i=1}^N {}^R X(r_i) \cdot \sum_{i=1}^N {}^E X(r_i)}{\sqrt{N \sum_{i=1}^N {}^R X(r_i)^2 - \left(\sum_{i=1}^N {}^R X(r_i) \right)^2} \cdot \sqrt{N \sum_{i=1}^N {}^E X(r_i)^2 - \left(\sum_{i=1}^N {}^E X(r_i) \right)^2}}. \quad (22)$$

Fig. 8 Reconstructed and simulated distributions of temperature and H₂O mole fraction at the equivalent ratio of 0.69 and the flow rate of shrouding nitrogen of 75 L/min. **a** and **b** show the distributions of temperature and H₂O mole fraction obtained using the 1D-WMST technique and the CFD simulation. **c** and **d** show the contours of temperature and H₂O mole fraction in the vertical section of the flame at $y = 0$ obtained by the CFD simulation



When the equivalent ratio was 0.69 and the flow rate of shrouding nitrogen was 22.5 L/min, F decreases from 0.96 to 0.88 as z increases from 10 to 40 mm, as shown in Fig. 7b, denoting that the premixed flame near the burner plug is more flat than that far from the burner plug.

3.4 Discussions

In practice, the flow rate of shrouding nitrogen plays an important role in affecting the flame flatness. To be specific, insufficient shrouding nitrogen will result in more intensive convection between the core flame and the surrounding air, while excessive shrouding nitrogen will increase heat loss and introduce distortion and fluctuation to the flame. To further validate the proposed technique, the following experiment was implemented on a non-flat flame, which was generated by increasing the flow rate of shrouding nitrogen. In this case, the equivalent ratio was kept at 0.69, while the flow rate of shrouding nitrogen was increased to 75 L/min. The mean values of the reconstructed ${}^R T(r_i)$ and ${}^R X(r_i)$ also agree well with the simulated ${}^S T(r_i)$ and ${}^S X(r_i)$ at $z = 40$ mm, as shown in Fig. 8a and b. Figure 8c and d shows the contours of temperature and H₂O mole fraction obtained from CFD simulation. Both the experimental and simulation results show that the distributions of temperature and H₂O mole fraction were non-uniform even in the core flame, denoting that the flame was non-flat. Moreover, the standard deviations of ${}^R T(r_i)$ and ${}^R X(r_i)$ are significantly larger than those in Fig. 7a and b, which are mainly caused by the distortion and instability of the flame in case of excessive shrouding nitrogen.

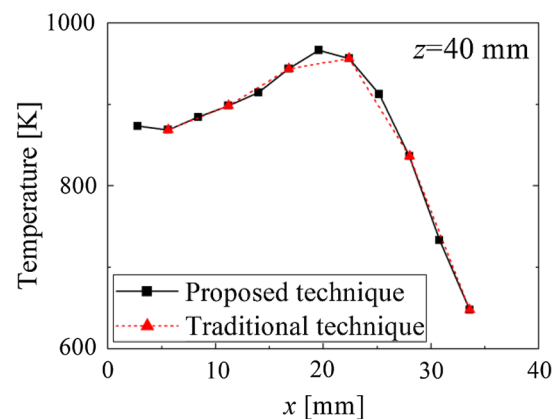


Fig. 9 With equivalent ratio of 0.69 and the flow rate of shrouding nitrogen of 75 L/min, comparison of the temperature distributions at $z = 40$ mm reconstructed using the resolution-doubled and traditional techniques, respectively

As shown in Fig. 9, by setting the same combustion conditions with those in Fig. 8, the mean values of ${}^R T(r_i)$ at $z = 40$ mm are retrieved using the resolution-doubled technique and the traditional technique, respectively. Constrained to the size of each collimator, six collimators can be placed in the left or right side of y axis in the real geometry. If the traditional one-dimensional tomography is adopted, the flame can only be discretized into six equal-spaced concentric circles, and thus, the tomographic resolution is 5.6 mm. In this way, the reconstructed profile from $x = 0$ to 35 mm is depicted by six points, which is too rough to depict the details of the reconstructed profile.

Using the proposed method, the reconstructed profile is depicted by 12 points, and thus, the tomographic resolution is up to 2.8 mm at the cost of 12 collimators placed on both sides of y axis. Obviously, the resolution-doubled technique is able to obtain more details of the reconstructed temperature distribution compared with the traditional technique.

In a case that higher tomographic resolution is needed, another group of parallel laser beams with same interval between two neighboring laser beams can be added at 90 degrees perpendicular to the current group. By adjusting the interval between l_1 in the added group and x axis to $\Delta r/4$, the tomographic resolution will be quadrupled up to $\Delta r/4$. However, when the computation domain is discretized into more annular elements, the solution will become more ill-posed, that is to say, small perturbations on the measurements will result in large perturbations on the reconstruction results [29]. In this case, regularization methods such as Tikhonov regularized decomposition can be used to increase the robustness of the solution and make the reconstructions less sensitive to measurement noises.

4 Conclusions

The resolution-doubled 1D-WMST technique was proposed to validate the flame flatness of the flat-flame burner in the paper. Using one view of multiple parallel laser beams, the distributions of temperature and H_2O mole fraction in the axisymmetric flame were simultaneously reconstructed. With the designed novel geometry of the parallel laser beams, a doubled tomographic resolution of $\Delta r/2$ was realized when the interval of two neighboring parallel laser beams was Δr . Furthermore, the flatness factor is quantitatively described by the similarity between the reconstructed and the expected distributions of H_2O mole fraction. The results show that the flame is more flat near the burner plug than that far from the burner plug, denoting that the proposed technique provides a noninvasive, reliable and low cost way to validate the flame flatness. Furthermore, the geometric design of the projections in the proposed technique can be applied to reconstruct the axisymmetric parameters and increase the tomographic resolution in other applications.

Acknowledgments The authors gratefully acknowledge the financial support from the National Science Foundation of China (Grant Nos. 61225006, 61327011 and 613111201) and the Program for Changjiang Scholars and Innovative Research Team in University (IRT1203).

References

1. J.F. Yu, R. Yu, X.Q. Fan, M. Christensen, A.A. Konnov, X.S. Bai, *Combust. Flame* **160**, 1276–1286 (2013)
2. A.A. Konnov, R. Riemeijer, V.N. Kornilov, L.P.H. de Goey, *Exp. Therm. Fluid Sci.* **47**, 213–223 (2013)
3. A. Matynia, J.L. Delfau, L. Pillier, C. Vovelle, *Combust. Explos. Shock Wave* **45**, 635–645 (2009)
4. G. Hartung, J. Hult, C.F. Kaminski, *Meas. Sci. Technol.* **17**, 2485–2493 (2006)
5. G. Sutton, A. Levick, G. Edwards, D. Greenhalgh, *Combust. Flame* **147**, 39–48 (2006)
6. R.D. Hancock, K.E. Bertagnolli, R.P. Lucht, *Combust. Flame* **109**, 323–331 (1997)
7. L. Xu, C. Liu, D. Zheng, Z. Cao, W. Cai, *Rev. Sci. Instrum.* **85**, 123108 (2014)
8. S. Prucker, W. Meier, W. Stricker, *Rev. Sci. Instrum.* **65**, 2908–2911 (1994)
9. A.A. Konnov, R. Riemeijer, L.P.H. de Goey, *Fuel* **89**, 1392–1396 (2010)
10. F. Migliorini, S. De Iulius, F. Cignoli, G. Zizak, *Combust. Flame* **153**, 384–393 (2008)
11. T. Fuyuto, H. Kronemayer, B. Lewerich, J. Brübach, T. Fujikawa, K. Akihama, T. Dreier, C. Schulz, *Exp. Fluids* **49**, 783–795 (2010)
12. H. Li, G.B. Rieker, X. Liu, J.B. Jeffries, R.K. Hanson, *Appl. Opt.* **45**, 1052–1061 (2006)
13. C.S. Goldenstein, R.M. Spearrin, I.A. Schultz, J.B. Jeffries, R.K. Hanson, *Meas. Sci. Technol.* **25**, 105104 (2014)
14. C.S. Goldenstein, I.A. Schultz, R.M. Spearrin, J.B. Jeffries, R.K. Hanson, *Appl. Phys. B* **116**, 717–727 (2014)
15. K. Sun, X. Chao, R. Sur, J.B. Jeffries, R.K. Hanson, *Appl. Phys. B* **110**, 497–508 (2013)
16. W. Cai, C.F. Kaminski, *Appl. Phys. Lett.* **104**, 154106 (2014)
17. W. Cai, C.F. Kaminski, *Appl. Phys. Lett.* **104**, 034101 (2014)
18. F. Wang, K.F. Cen, N. Li, J.B. Jeffries, Q.X. Huang, J.H. Yan, Y. Chi, *Meas. Sci. Technol.* **21**, 045301 (2010)
19. L. Ma, W. Cai, *Opt. Express* **17**, 8602–8613 (2009)
20. S. Pal, K.B. Ozanyan, H. McCann, *Meas. Sci. Technol.* **19**, 094018 (2008)
21. M.M. Hossain, G. Lu, D. Sun, Y. Yan, *Meas. Sci. Technol.* **24**, 074010 (2013)
22. C.J. Dasch, *Appl. Opt.* **31**, 1146–1152 (1992)
23. C. Liu, L. Xu, Z. Cao, H. McCann, *Instrum. Meas. IEEE Trans.* **63**, 3067–3075 (2014)
24. C.S. Goldenstein, C.L. Strand, I.A. Schultz, K. Sun, J.B. Jeffries, R.K. Hanson, *Appl. Opt.* **53**, 356–367 (2014)
25. K. Sun, X. Chao, R. Sur, C.S. Goldenstein, J.B. Jeffries, R.K. Hanson, *Meas. Sci. Technol.* **24**, 125203 (2013)
26. S.A. Tsekenis, N. Tait, H. McCann, *Rev. Sci. Instrum.* **86**, 035104 (2015)
27. F. Li, X. Yu, H. Gu, Z. Li, Y. Zhao, L. Ma, L. Chen, X. Chang, *Appl. Opt.* **50**, 6697–6707 (2011)
28. H. Yang, D. Greszik, T. Dreier, C. Schulz, *Appl. Phys. B* **99**, 385–390 (2010)
29. E.O.A. Kesson, K.J. Daun, *Appl. Opt.* **47**, 407–416 (2008)